Self-pulsing in Tm-doped $YAlO_3$ lasers: Excited-state absorption and chaos

Ka S. Wu, Ori Henderson-Sapir, Peter J. Veitch, Murray Hamilton, Jesper Munch, and David J. Ottaway
School of Physical Sciences and Institute for Photonics & Advanced Sensing (IPAS), The University of Adelaide, Adelaide 5005, Australia
(Received 29 July 2014; published 13 April 2015)

Tm:$YAlO_3$ lasers suffer from self-pulsing. A four-level rate equation analysis suggested that the self-pulsing could be due to excited-state absorption. We report a measurement of the cross section for this absorption and show that it is too small to be the sole cause of the self-pulsing. We propose nonlinear dynamical chaos as an alternative explanation and present a chaos analysis of the output of a cw-pumped Tm:$YAlO_3$ laser, including experimental evidence of chaos.

DOI: 10.1103/PhysRevA.91.043819 PACS number(s): 42.60.Mi, 42.70.Hj, 78.20.Ci

I. INTRODUCTION

The development of lasers operating at wavelengths near 2 μm is of importance to many fields, such as medicine, remote sensing, and fundamental research. Tm:$YAlO_3$ (or Tm:YAP) lasers are of particular interest due to their high efficiency [1], excellent thermomechanical properties, and natural birefringence of the crystal. A major drawback of Tm:$YAlO_3$ lasers is their tendency to self-pulse, even under continuous-wave (cw) pumping [2–4], as shown in Fig. 1. This instability, along with the high peak powers associated with the self-pulsing, limits the usefulness of Tm:$YAlO_3$ lasers.

The origin of the self-pulsing is not well understood, although it has been suppressed using various types of feedback, including using intracavity acousto-optic modulators [2,3] and pump diode current actuation [4]. A number of mechanisms have been proposed to explain the self-pulsing in Tm:$YAlO_3$ lasers, such as pump power fluctuations [5], mechanical instabilities, and saturable absorption by water in the air of the laser resonator [6]. However, these explanations do not explain the observation of self-pulsing in all cases. For example, while Šulc *et al.* [6] observed that the output of their monolithic Tm:$YAlO_3$ laser was stable over a broad range of pump powers, Razdobreev and Shestakov [7] observed that the output of their monolithic laser pulsed regularly at higher pump powers.

Razdobreev and Shestakov [7] presented a rate equation model that showed the pulsing could be explained by including excited-state absorption (ESA) of photons at the lasing wavelength by the transition $^3H_5 \rightarrow {}^3H_4$. This model assumed an ESA to emission cross-section ratio of $\gamma = \sigma_{\mathrm{ESA}}/\sigma \approx 0.65$. They also pointed out that the measurement of the ESA cross section had not yet been performed and was required to verify the model.

Self-pulsing behavior in a laser may also be explained by nonlinear dynamics with chaotic solutions [8–12]. Of particular interest is the NH_3 laser [13,14], which can be made to exhibit self-pulsing without any external perturbations. The self-pulsing of our Tm:$YAlO_3$ laser [4] is remarkably similar to that of chaotic NH_3 lasers [8,13]. Additionally, the observation of two distinct dynamical regimes by Razdobreev and Shestakov [7], namely, a stable cw output at low pump power and robust self-pulsing beyond a certain threshold, is consistent with an explanation in terms of nonlinear dynamic systems.

We report here an investigation of the self-pulsing. We first describe measurement of the cross section for the ESA transition $^3H_5 \rightarrow {}^3H_4$ and show that it is too small to account solely for the self-pulsing in Tm:$YAlO_3$ lasers. We then show that the self-pulsing is consistent with nonlinear dynamical chaos. Here chaos has been observed in a simple solid-state crystal laser without any external perturbations or other nonlinear optical elements.

II. EXCITED-STATE ABSORPTION

The energy-level diagram of Tm:$YAlO_3$ is shown in Fig. 2. The ESA can be observed by using a short pump pulse to excite Tm^{3+} ions to the $^3H_5$ level and a cw probe beam at the lasing wavelength to observe the resulting change in the upper $^3F_4$ lasing manifold, as explained below.

The equilibrium transmittance of the probe beam through the Tm:$YAlO_3$ crystal prior to the pump pulse is given by

$$T_{eq} = \exp(\sigma[f_u N_2 - f_l(N - N_2)]l) \tag{1a}$$

$$\approx \exp(-\sigma f_l N l) \quad \text{for} \quad N_2 \ll N, \tag{1b}$$

where σ is the cross section for transitions at the probe wavelength between the ground state and the $^3F_4$ manifold, f_u and f_l are the Boltzmann factors for the $^3F_4$ manifold and ground state, respectively, N is the total Tm^{3+} ion density, N_2 is the equilibrium density in the $^3F_4$ manifold, and l is the length of the crystal.

During the pump pulse, ΔN ground-state ions are excited to the $^3H_5$ level. The absorption at the probe wavelength changes due to this excitation, as the excited ions no longer contribute to the ground-state absorption (GSA) but can instead contribute to ESA. The transmittance of the probe beam immediately after the pump pulse is given by

$$T_{ns} = T_{eq} \exp([\sigma f_l - \sigma_{\mathrm{ESA}}]\Delta N l), \tag{2}$$

where σ_{ESA} is the effective cross section for absorption of a probe photon by an ion in the $^3H_5$ level. If $\sigma_{\mathrm{ESA}} > \sigma f l$ as expected, then the pump pulse will result in a sudden decrease in probe transmittance, as illustrated in Fig. 3.

Ions in the $^3H_5$ level will readily decay nonradiatively to the $^3F_4$ manifold as the energy gap between the $^3H_5$ and $^3F_4$ levels is readily bridged by phonons, resulting in a predicted lifetime of the $^3H_5$ level on the microsecond scale [15]. However, some of the ions will absorb a probe photon and be excited to the $^3H_4$ level via ESA. The majority of these ions will then cross-relax to the $^3F_4$ level [16].

This cross relaxation results in additional ions being excited to the $^3F_4$ manifold from the ground state, which is undesirable

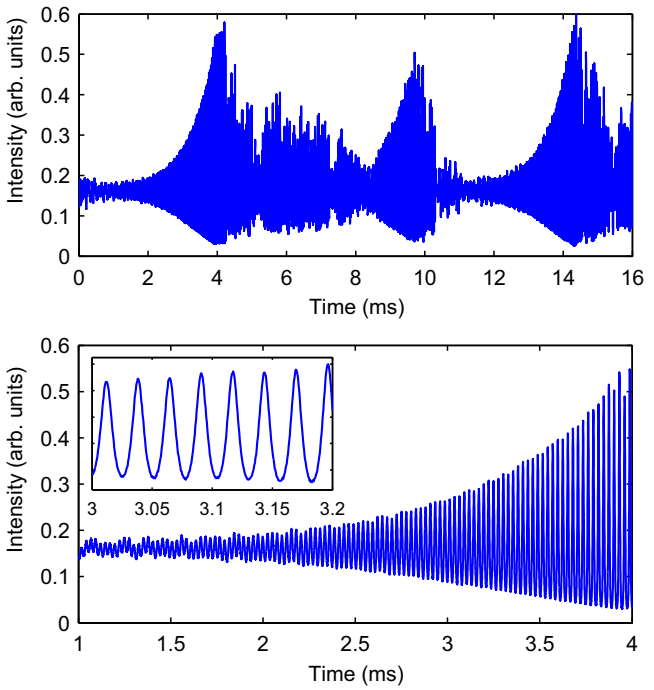

FIG. 1. (Color online) Typical output of a Tm:$YAlO_3$ laser (top), with a plot of a single "burst" with improved temporal resolution (bottom) and the underlying oscillations (inset).

in this experiment as it introduces uncertainty in the population density of the $^3F_4$ manifold. To ensure nonradiative decay is the dominant process, the probe beam needs to be sufficiently weak to minimize the number of ions that undergo ESA, but still strong enough to provide an adequate signal. The transmittance of the probe beam after the decay of the $^3H_5$ population is given by

$$T_{\mu s} \approx T_{eq} \exp(\sigma[f_u + f_l]\Delta N l). \tag{3}$$

The ions in the $^3H_4$ manifold then gradually decay back to the ground state and the system relaxes back to its equilibrium

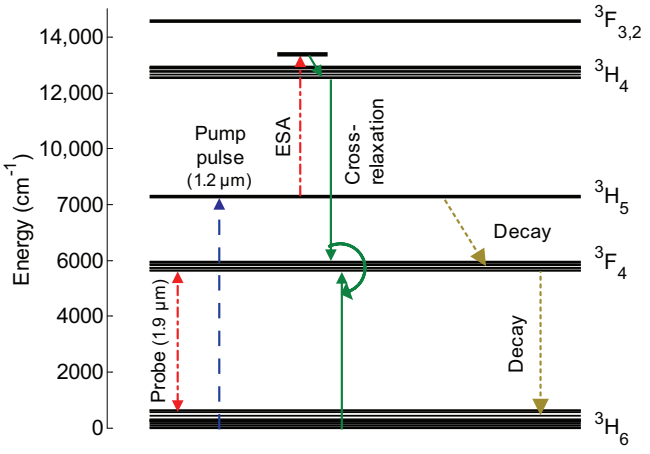

FIG. 2. (Color online) Energy-level diagram of Tm:$YAlO_3$, with the two main avenues for ions in $^3H_5$ to de-excite: ESA followed by cross relaxation, or nonradiative decay $^3H_5 \rightarrow {}^3F_4$.

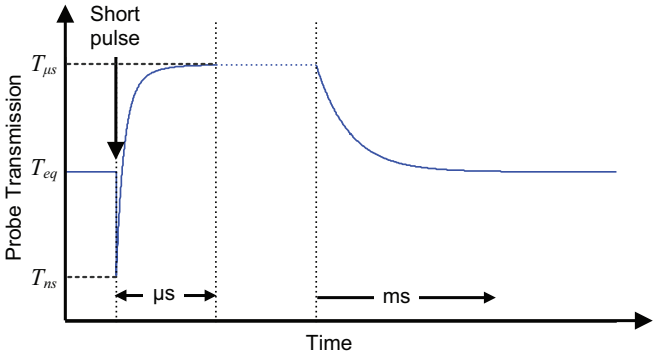

FIG. 3. (Color online) Expected probe transmittance trace during and after the short pump pulse.

state. Since the transitions of the Tm^{3+} ions occur at different time scales, they can be distinguished.

The ratio between the ESA and laser emission cross sections can be determined from the measurement of the changes in probe transmittance. If $\Delta N \ll |(\sigma[f_u + f_l]l)^{-1}|$ and $\Delta N \ll |([\sigma f_l - \sigma_{\mathrm{ESA}}]l)^{-1}|$, then the approximation $e^x \approx 1 + x$ can be applied to Eq. (3) and Eq. (2), giving

$$\Delta N = \frac{1}{\sigma(f_u + f_l)l}\left(\frac{T_{\mu s} - T_{eq}}{T_{eq}}\right), \tag{4}$$

and

$$\gamma = \frac{\sigma_{\mathrm{ESA}}}{\sigma} \approx f_l - \frac{1}{\sigma \Delta N l}\left(\frac{T_{ns} - T_{eq}}{T_{eq}}\right) \tag{5a}$$

$$= f_l - (f_u + f_l)\left(\frac{T_{ns} - T_{eq}}{T_{\mu s} - T_{eq}}\right). \tag{5b}$$

Assuming linearity of the detector, the ratio of the transmittance change is given by the ratio of the voltage change, further simplifying Eq. (5b):

$$\gamma = f_l - (f_u + f_l)\left(\frac{\Delta V_{ns}}{\Delta V_{\mu s}}\right), \tag{6}$$

where $\Delta V_{ns} = D(T_{ns} - T_{eq})P$ and $\Delta V_{\mu s} = D(T_{\mu s} - T_{eq})P$. Here, D is the detector constant and P is the probe power incident on the crystal. Equation (1b) can be used to determine the cross section σ and hence the ESA cross section σ_{ESA}.

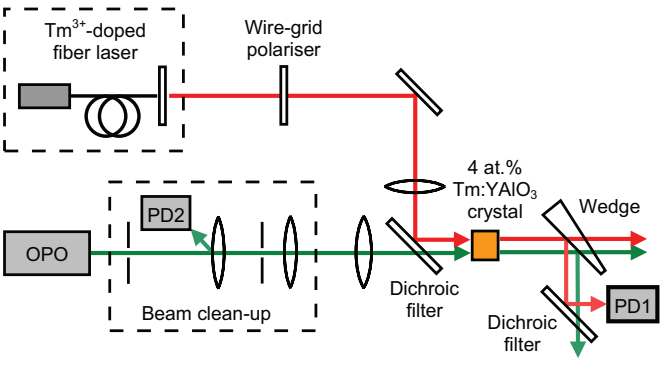

FIG. 4. (Color online) Schematic of the measurement system.

A schematic of the measurement system is shown in Fig. 4. An a-cut Tm:$YAlO_3$ crystal (4 at%) with dimensions 4.55 $\times$ 5.02 $\times$ 5.54 mm along the crystalline a, b, and c axes, respectively, was used. The end faces were antireflective coated for the pump and probe wavelengths.

The probe beam was generated by a Tm^{3+}-doped fiber laser at 1.944 μm that was stabilized by a fiber Bragg grating. Although this fiber laser operated at a slightly longer wavelength than the Tm:$YAlO_3$ peak emission wavelength of 1.940 μm, the energy difference of 10.6 cm^{-1} is negligible compared to the spread in energy of the Stark sublevels of the $^3H_4$ level and the phonon energies in $YAlO_3$, which are both of the order of 100 cm^{-1} [17,18]. A wire-grid polarizer with an extinction ratio of >1500 was used to ensure that the probe light incident on the Tm:$YAlO_3$ was polarized along the c axis, as observed during lasing [1]. The fiber laser was operated at an output power of 300 mW, which resulted in ~0.1% of ions in the $^3F_4$ level at steady state, satisfying the requirement for the approximation for Eq. (1b). Furthermore, it was calculated that negligible amounts of ions in the $^3H_5$ level after the pump pulse would undergo ESA due to the low intensities.

An optical parametric oscillator (OPO) was used to generate pump pulses with a duration of less than 10 ns at 1.21 μm for excitation of the $^3H_6 \rightarrow {}^3H_5$ transition. A spatial filter was used to improve the beam quality. The pulse energy incident on the crystal was 0.8 mJ. Approximately 2.2×10^{19} cm^{-3} or 2.8% of the total ions are excited by the OPO pulse. This satisfies the approximation condition for Eq. (4), as it is 2 orders of magnitude less than the term on the right-hand side.

The two beams were combined using a dichroic mirror, which was highly reflective (HR) at 1.94 μm and antireflective (AR) at 1.2 μm. The two beams were focused independently into the Tm:$YAlO_3$ crystal, and both had a beam diameter of 250 μm at the focus as measured by a pyroelectric camera. The camera was also used to align the two beams by overlapping the beam profiles.

The transmitted probe beam power was measured using an extended-InGaAs photodetector (PD1) with a rise time <250 ns. A wedge was used to reduce the power. The pump pulse was further attenuated using a dichroic mirror and long-pass filters (wavelength cutoff at 1500 nm). An InGaAs photodetector (PD2) with a rise time of less than 10 ns (Thorlabs DET10C) was used to detect the pulse from the OPO from scattered light and trigger the oscilloscope.

The time dependence of the transmitted probe beam for the microsecond and millisecond time scales is shown in Figs. 5 and 6, respectively. To increase the signal to noise of the measurement, the traces shown were averaged over 128 pulses. As expected, the transmittance increases exponentially with a microsecond time constant after the pump pulse, followed by an exponential decrease.

The increase in the probe transmittance on the microsecond time scale (shown in Fig. 5) corresponds to the decay $^3H_5 \rightarrow {}^3F_4$, which has a fitted time constant of 440 $\pm$ 5 ns. Note that the data earlier than 0.25 μs was not included in the fit due to electronic ringing, which is responsible for the sudden increase in transmittance near $t = 0$. The measurement of this time constant is approximately consistent with the calculated value from literature [15].

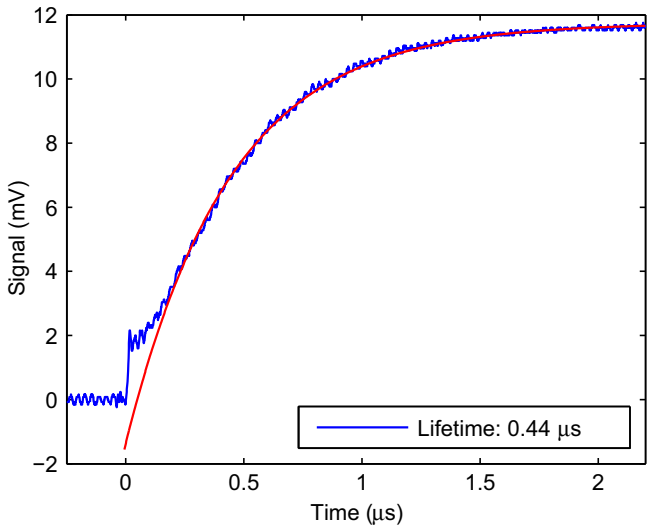

FIG. 5. (Color online) Probe beam signal from the ac-coupled detector PD1 in the microsecond range, with an exponential fit.

The decrease of transmittance in the millisecond time scale (shown in Fig. 6) corresponds to the transition $^3F_4 \rightarrow {}^3H_6$, which has a fitted time constant of $\tau = 3.35 \pm 0.05$ ms. This time constant is shorter than the spontaneous lifetime from literature [19], and this is due to stimulated emission induced by the incident probe beam. When the stimulated emission rate was subtracted from the total decay rate (determined from the fitted time constant), the spontaneous decay rate was consistent with that in the literature.

The expected instantaneous decrease in transmitted probe power following the pump pulse was obscured by some electronic ringing of the photodetector following the pump pulse. However, the instantaneous decrease can be estimated by extrapolating the exponential fit of the decay curve to $t = 0$. This result was checked by subtracting from the measured curve the temporal profile of the pump leakage measured with

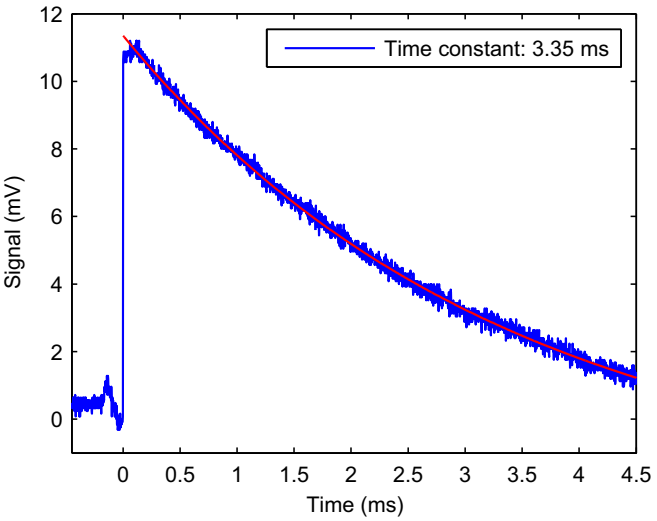

FIG. 6. (Color online) Probe beam signal from the ac-coupled detector PD1 in the millisecond range, with an exponential fit.

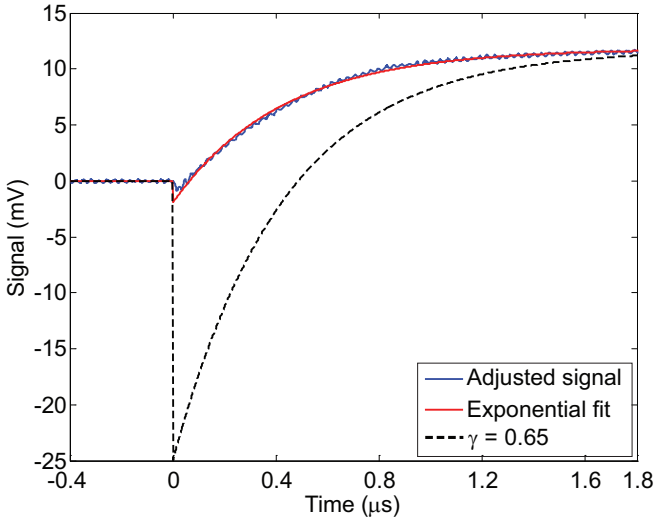

FIG. 7. (Color online) Corrected experimental trace (blue) and exponential fit (red), compared to the theoretical decay curve for a voltage drop of 25 mV corresponding to $\gamma = 0.65$ (black).

no probe. The resulting corrected signal is shown in Fig. 7, showing a small drop in the instantaneous transmittance.

The voltage changes from the steady state were estimated as shown in Fig. 5, giving $\Delta V_{ns} = 2 \pm 0.25$ mV and $\Delta V_{\mu s} = 11.75 \pm 0.25$ mV. The value of ΔN was calculated from $\Delta V_{\mu s}$ and the equilibrium dc voltage of 460 mV to be $3.1 \pm 0.3\%$ of the total number of ions. This is consistent with that calculated from the pump-pulse absorption, confirming good overlap of the two beams. Using the Boltzmann factors $f_u = 0.263$ and $f_l = 0.03$ [7], the ratio of ESA to GSA cross sections $\gamma = 0.08 \pm 0.01$.

The cross section σ for the absorption of the probe beam was calculated from the steady-state GSA of the probe beam using Eq. (1a), assuming $N_2 \ll N$. For a measured $T_{eq} = 0.920 \pm 0.005$, and $N = 7.8 \times 10^{20}$ cm^{-3} and $l = 0.455 \pm 0.001$ cm, the cross section $\sigma = (7.8 \pm 0.5) \times 10^{-21}$ cm^2. The ESA cross section is therefore $\sigma_{\mathrm{ESA}} = \gamma\sigma = (6.3 \pm 0.7) \times 10^{-22}$ cm^2.

Our measured value of γ is much less than that used in the model of Razdobreev and Shestakov [7]. To confirm that it would result in a stable cw output, we reproduced their model and used parameters for the laser in our previous work [4]. cw output was observed in the model even when various parameters were changed by a factor of 2, including the cross section, cross relaxation, and decay rates, pump rate, and cavity time constant. To further emphasize the robustness of our measurement, we compare the measured pump-probe temporal response with that predicted for $\gamma = 0.65$, as shown in Fig. 7.

It is thus clear that the rate equation model of Razdobreev and Shestakov would yield a stable cw output and is not by itself an explanation of the pulsing in Tm:$YAlO_3$.

III. CHAOTIC LASER DYNAMICS

The Tm:$YAlO_3$ laser described in our previous work [4] was reassembled to obtain the data for the analysis presented here. The laser was a simple crystal laser, pumped by a 790-nm fiber-coupled diode. The crystal from the ESA measurement was used as the gain medium. The resonator consisted of a flat, high-reflectivity mirror, the laser crystal, an intracavity lens to compensate for thermal lensing, and a flat output coupler with a reflectivity of 95% at 1.94 μm. The laser exhibited similar, exponentially growing bursts of oscillations, as presented in our previous work [4].

The output was measured using an extended-range InGaAs photodetector with a 25-ns rise/fall time, and digitized using a 2-MS/s oscilloscope, giving 32,000 points. The full data set is shown in Fig. 1. We describe below analyses of this data using two standard tests for chaotic dynamics: phase-space reconstruction [20,21], and the 0–1 test for chaos [22,23].

Time delay embedding [20] was used to reconstruct the phase-space trajectories to determine the nature of the system dynamics. This method uses the data set I_n and its time-delayed versions to construct vectors in a d-dimensional Euclidean space:

$$\boldsymbol{y}(k) = [I_k, I_{k+\Delta n}, \ldots I_{k+(d-1)\Delta n}]. \tag{7}$$

These vectors define a trajectory that is topologically equivalent to the trajectory in the space of the actual physical variables. For sufficiently large d, the properties of the dynamic system are preserved and the trajectory is fully contained, or embedded, in this reconstruction of the phase space.

The delay Δn that would expand the trajectory maximally in the embedding space was determined using the average mutual information of the data set, which is given by

$$I_M(\Delta n) = \sum_k p(I_k, I_{k+\Delta n}) \log \left[\frac{p(I_k, I_{k+\Delta n})}{p(I_k)p(I_{k+\Delta n})} \right], \tag{8}$$

where $p(I_k, I_{k+\Delta n})$ is the joint probability distribution function and $p(I_k)$ and $p(I_{k+\Delta n})$ are the marginal probability distribution functions [21].

A minimum of I_M means that points in the time series, spaced by the corresponding delay, are as statistically independent as possible. When data spaced by this delay are used as coordinate values in the phase-space reconstruction, the coordinate axes are as close to orthogonal as possible. The optimum delay is chosen as the first minimum of I_M [21]. A plot of the average mutual information for different values of Δn is shown in Fig. 8, with the first minimum of I_M corresponding to $\Delta n = 13$.

The minimum number of dimensions required to embed the trajectory, without crossings, was obtained by calculating the fraction of false nearest neighbors for increasing dimensions [21]. The process is summarized in Appendix A. The trajectory is fully unfolded when the number of false neighbors reaches zero. The percentage of false neighbors in our data set, plotted in Fig. 9, reduces to 0.4% for embedding dimensions of 5, and remains approximately 0.2% for higher dimensions due to noise.

The three-dimensional (3D) projection of the reconstructed trajectory with an embedding dimension of 5 is shown in Fig. 10. The points of the reconstructed trajectory lie in a manifold of limited dimensionality, as shown in Fig. 10. A limited dimensionality implies dynamics with a limited number of physical variables, or degrees of freedom, and

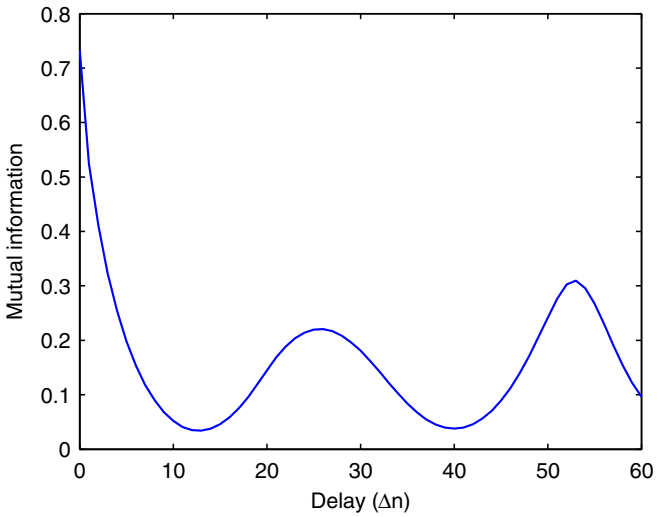

FIG. 8. (Color online) Average mutual information for different delays.

because the trajectory appears nonperiodic and is dense in the manifold, chaos is implied.

The dynamics of the time series were also investigated using the "0–1" test for chaos developed by Gottwald and Melbourne [22,23], which is summarized in Appendix B. This is a binary test that can distinguish between regular and chaotic dynamics in deterministic dynamical systems, even in the presence of moderate levels of noise [22]. The 0–1 test does not require the choice of parameters such as the delay and embedding dimension. The output of the test is a value $0 \leqslant K \leqslant 1$, corresponding to a linear correlation coefficient. For a sufficiently large number of samples $\mathcal{N}$ in the data set, $K = 0$ corresponds to regular dynamics and $K = 1$ corresponds to chaotic dynamics.

The 0–1 test was applied to the laser output data set and yielded $K = 0.99$, indicating that the pulsing is due to chaotic dynamics. This is consistent with the results from the phase-space reconstruction.

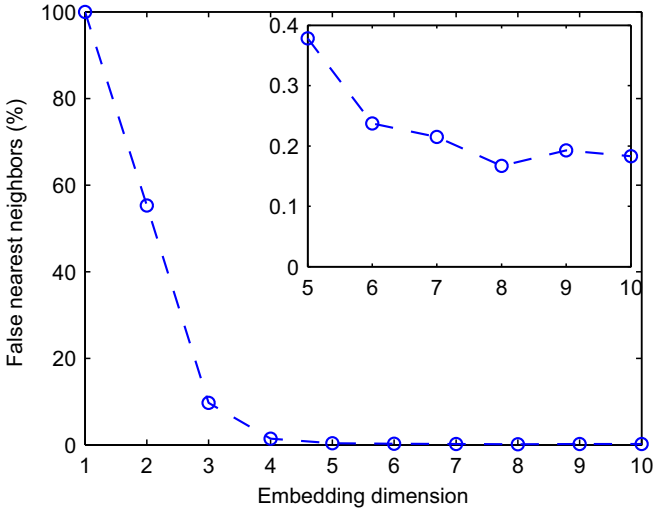

FIG. 9. (Color online) False nearest neighbors for increasing embedding dimensions.

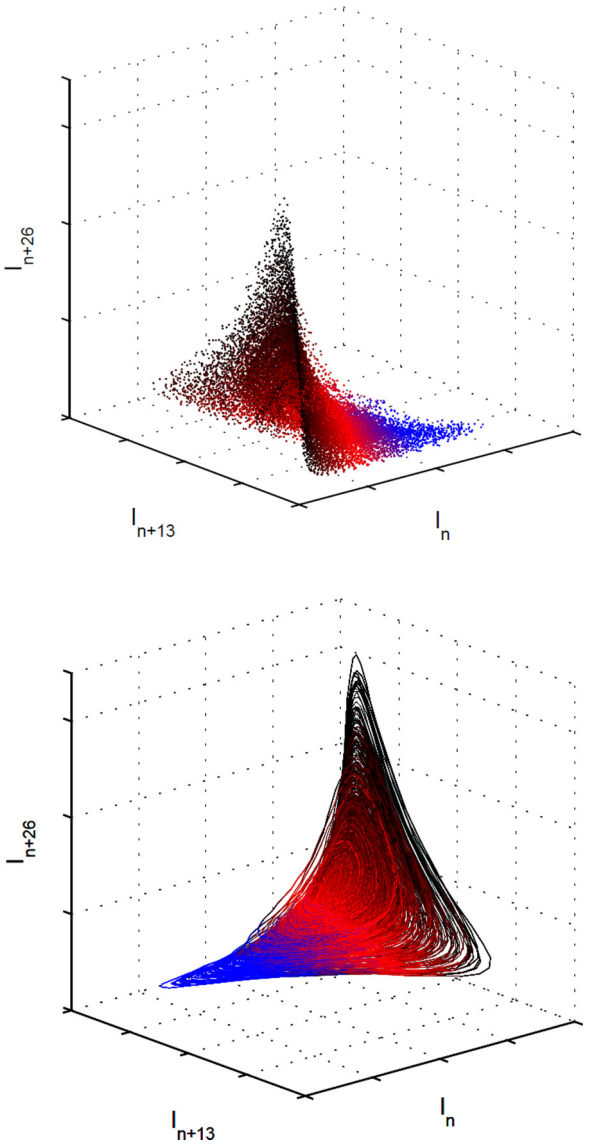

FIG. 10. (Color online) 3D projection of the phase-space structure from opposing angles, showing a trajectory of bound dimensionality (top) with dense, nonperiodic orbits (bottom). The color variations along I_n are for ease of viewing purposes only.

IV. CONCLUSIONS

We have shown that the self-pulsing in cw-pumped Tm:$YAlO_3$ lasers cannot be explained solely by the $^3H_5 \rightarrow {}^3H_4$ excited-state absorption suggested by Razdobreev and Shestakov [7], and is the result of chaotic dynamics in the laser. While chaotic behavior has been observed in more complex solid-state lasers involving known perturbations or intracavity nonlinearities [10–12], this is an example of chaos in a simple solid-state crystal laser without any external perturbations or other nonlinear optical elements.

The absence of any external perturbations for unstable pulsing in the Tm:$YAlO_3$ laser makes it comparable to a

chaotic class-C laser, with three or more coupled variables that have similar relaxation time constants [24]. Chaotic class-C lasers naturally have a second threshold for the onset of chaos above the lasing threshold [9]. This is consistent with the presence of two distinct dynamical regimes, as observed by Razdobreev and Shestakov [7]. However, the physical parameters responsible for the chaotic behavior are currently unknown. Typically, chaotic class-C lasers require the lifetimes of the polarization, inversion, and cavity field to be of the same order of magnitude. However in Tm:$YAlO_3$ lasers, the inversion lifetime is of the order of milliseconds, while the cavity field lifetime is of the order of nanoseconds; the polarization lifetime in $YAlO_3$ has not been measured to the best of our knowledge. Thus, there are likely additional parameters involved, and further investigation is necessary to identify them. Despite the parameters being unknown, we have demonstrated in our previous work that the chaotic behavior can be suppressed to a steady, cw state by controlling the inversion via proportional feedback to the pump diode laser [4].

ACKNOWLEDGMENTS

The authors would like to acknowledge Alexandre Francois for his assistance with the OPO. This work was supported by the South Australian Government through the Premier's Science and Research Fund.

APPENDIX A: CALCULATION OF FALSE NEAREST NEIGHBORS

The percentage of false nearest neighbors in dimension d is determined using the following process [21]:

(i) In dimension d, for each vector

$$\boldsymbol{y}(k) = [I_k, I_{k+\Delta n}, \ldots I_{k+(d-1)\Delta n}], \tag{A1}$$

calculate the Euclidean distance R_d to every other vector in dimension d, given by

$$R_d(k,k')^2 = \sum_{l=0}^{d-1} [I_{k+l\Delta n} - I_{k'+l\Delta n}]^2. \tag{A2}$$

(ii) Identify the nearest neighbor $\boldsymbol{y}(k_N)$ with the smallest R_d, and calculate the Euclidean distance between $\boldsymbol{y}(k)$ and $\boldsymbol{y}(k_N)$ in dimension $d+1$:

$$R_{d+1}(k,k_N)^2 = R_d(k,k_N)^2 + [I_{k+d\Delta n} - I_{k_N+d\Delta n}]^2. \tag{A3}$$

(iii) Determine whether $\boldsymbol{y}(k)$ and $\boldsymbol{y}(k_N)$ are true or false nearest neighbors; if

$$\frac{|I_{k+d\Delta n} - I_{k_N+d\Delta n}|}{R_d(k,k_N)} > R_T, \tag{A4}$$

where $R_T \in [10,50]$ is some fixed threshold value ($R_T = 15$ was used in our analysis), then $\boldsymbol{y}(k)$ and $\boldsymbol{y}(k_N)$ are considered false neighbors.

(iv) Repeat (i)–(iii) for all vectors in dimension d.

APPENDIX B: CALCULATION OF K IN THE "0–1" TEST

The value of K in the 0–1 test was determined using the following process [22,23]:

(i) For the data set I of size $\mathcal{N}$, define

$$p_c(n) = \sum_{k=1}^{n} I_k \cos(kc), \quad q_c(n) = \sum_{k=1}^{n} I_k \sin(kc), \tag{B1}$$

where $n = 1,2,\ldots\mathcal{N}$ and $c \in (\pi/5, 4\pi/5)$ is a randomly generated phase.

(ii) Define the modified mean-square displacement:

$$D_c(n) = M_c(n) - V_{\mathrm{osc}}(c,n), \tag{B2}$$

where $M_c(n)$ is the mean-square displacement, given by

$$M_c(n) = \frac{1}{\mathcal{N}} \sum_{l=1}^{\mathcal{N}} [p_c(n+l) - p_c(l)]^2 + [q_c(n+l) - q_c(l)]^2, \tag{B3}$$

and

$$V_{\mathrm{osc}}(c,n) = \left[\frac{1}{\mathcal{N}} \sum_{k=1}^{\mathcal{N}} I_k\right]^2 \frac{1-\cos nc}{1-\cos c}. \tag{B4}$$

(iii) Calculate the linear correlation coefficient K_c of $D_c(n)$:

$$K_c = \mathrm{corr}(n, D(n)) \quad \text{for} \quad n = 1,2,\ldots\mathcal{N}/10. \tag{B5}$$

(iv) Repeat (i)–(iii) for 100 randomly generated values of c to prevent resonance phenomena when $\mathcal{N}$ is small. K is then defined as the median value of $\{K_c\}$.

[1] R. C. Stoneman and L. Esterowitz, Efficient 1.94-μm Tm:YALO laser, IEEE J. Sel. Top. Quantum Electron. **1**, 78 (1995).

[2] P. Černý, G. J. Valentine, and D. Burns, Actively stabilised diode pumped Tm:YAlO laser, Electron. Lett. **40**, 1061 (2004).

[3] A. C. Sullivan, A. Zakel, G. J. Wagner, D. Gwin, B. Tiemann, R. C. Stoneman, and A. I. R. Malm, High power Q-switched Tm: YALO lasers, OSA Proc. Adv. Solid-State Photonics **19**, 329 (2004).

[4] K. S. Wu, P. J. Veitch, J. Munch, and D. J. Ottaway, Suppression of self-pulsing in Tm:$YAlO_3$ lasers via current feedback, Appl. Phys. B **114**, 415 (2013).

[5] I. F. Elder and M. J. P. Payne, Lasing in diode-pumped Tm:YAP, Tm, Ho:YAP and Tm, Ho:YLF, Opt. Commun. **145**, 329 (1998).

[6] J. Šulc, H. Jelínková, K. Nejezchleb, and V. Škoda, Fluctuation-free CW Tm:YAP laser with monolithic resonator, in *European Conference on Lasers and Electro-Optics 2009 and the European Quantum Electronics Conference, CLEO Europe - EQEC 2009, Munich*, Vol. 269 (IEEE, Piscataway, NJ, 2009), p. 1.

[7] I. Razdobreev and A. Shestakov, Self-pulsing of a monolithic Tm-doped $YAlO_3$ microlaser, Phys. Rev. A **73**, 053815 (2006).

[8] C. Weiss, Chaotic laser dynamics, Opt. Quantum Electron. **20**, 1 (1988).

[9] J. Ohtsubo, *Semiconductor Lasers - Stability, Instability and Chaos*, 3rd ed. (Springer-Verlag, Berlin, 2013).

[10] E. A. Viktorov and P. Mandel, Low frequency fluctuations in a multimode semiconductor laser with optical feedback, Phys. Rev. Lett. **85**, 3157 (2000).

[11] P. Mandel and X.-G. Wu, Second-harmonic generation in a laser cavity, J. Opt. Soc. Am. **3**, 940 (1986).

[12] E. M. Pessina, G. Bonfrate, F. Fontana, and L. A. Lugiato, Experimental observation of the Risken-Nummedal-Graham-Haken multimode laser instability, Phys. Rev. A **56**, 4086 (1997).

[13] C. O. Weiss and J. Brock, Evidence for Lorenz-type chaos in a laser, Phys. Rev. Lett. **57**, 2804 (1986).

[14] C. O. Weiss, U. Hübner, N. B. Abraham, and D. Tang, Lorenz-like chaos in NH_3-FIR lasers, Infrared Phys. Technol. **36**, 489 (1995).

[15] J. A. Caird, L. G. DeShazer, and J. Nella, Characteristics of room-temperature 2.3-μm laser emission from Tm^{3+} in YAG and $YAlO_3$, IEEE J. Quantum Electron. **11**, 874 (1975).

[16] N. Borodin, P. Kryukov, and A. Popov, Diode-pumped cw Tm^{3+} : $YAlO_3$ laser, Quantum Electron. **35**, 511 (2005).

[17] M. J. Weber, Multiphonon relaxation of rare-earth ions in yttrium orthoaluminate, Phys. Rev. B **8**, 54 (1973).

[18] M. Eichhorn, Quasi-three-level solid-state lasers in the near and mid infrared based on trivalent rare earth ions, Appl. Phys. B **93**, 269 (2008).

[19] I. F. Elder and M. J. P. Payne, Comparison of diode-pumped Tm:YAP with Tm:YAG, OSA Proc. Adv. Solid-State Lasers **19**, ML6 (1998).

[20] F. Takens, in *Dynamical Systems and Turbulence*, edited by D. Rand and L.-S. Young, Lecture Notes in Mathematics, Vol. 898 (Springer, Berlin, 1981), pp. 366–381.

[21] H. D. Abarbanel, R. Brown, J. J. Sidorowich, and L. S. Tsimring, The analysis of observed chaotic data in physical systems, Rev. Mod. Phys. **65**, 1331 (1993).

[22] G. A. Gottwald and I. Melbourne, Testing for chaos in deterministic systems with noise, Phys. D (Amsterdam, Neth.) **212**, 100 (2005).

[23] G. A. Gottwald and I. Melbourne, On the implementation of the 0-1 test for chaos, SIAM J. Appl. Dynamical Systems **8**, 129 (2009).

[24] F. T. Arecchi, G. L. Lippi, G. P. Puccioni, and J. R. Tredicce, Deterministic chaos in laser with injected signal, Opt. Commun. **51**, 308 (1984).